



Basic characterization of TORPEX electrostatic modes in closed field line configurations

F. Avino, A. Fasoli, I. Furno, S. Jolliet, and P. Ricci

Citation: [Physics of Plasmas \(1994-present\)](#) **21**, 122115 (2014); doi: 10.1063/1.4904808

View online: <http://dx.doi.org/10.1063/1.4904808>

View Table of Contents: <http://scitation.aip.org/content/aip/journal/pop/21/12?ver=pdfcov>

Published by the [AIP Publishing](#)

Articles you may be interested in

[Microturbulence in DIII-D tokamak pedestal. I. Electrostatic instabilities](#)

Phys. Plasmas **21**, 042110 (2014); 10.1063/1.4871387

[Multiscale coherent structures in tokamak plasma turbulence](#)

Phys. Plasmas **13**, 102509 (2006); 10.1063/1.2357045

[Experimental characterization of drift-interchange instabilities in a simple toroidal plasma](#)

Phys. Plasmas **13**, 102104 (2006); 10.1063/1.2356483

[Electrostatic drift modes in a closed field line configuration](#)

Phys. Plasmas **9**, 395 (2002); 10.1063/1.1431594

[Electromagnetic ion-temperature-gradient modes and anomalous transport in a nonuniform magnetized plasma with equilibrium flows](#)

Phys. Plasmas **7**, 1125 (2000); 10.1063/1.873920



Basic characterization of TORPEX electrostatic modes in closed field line configurations

F. Avino,^{a)} A. Fasoli, I. Furno, S. Jolliet, and P. Ricci

Centre de Recherches en Physique des Plasmas (CRPP), Ecole Polytechnique Fédérale de Lausanne (EPFL), Association Euratom-Confédération Helvétique, CH-1015 Lausanne, Switzerland

(Received 3 October 2014; accepted 5 December 2014; published online 23 December 2014)

Electrostatic coherent modes are studied in the TORPEX device [Fasoli *et al.*, Plasma Phys. Controlled Fusion **52**, 124020 (2010)], in closed flux surfaces. The accessibility to this magnetic geometry is provided by a current-carrying in-vessel toroidal conductor developed to generate a poloidal magnetic field [Avino *et al.*, Rev. Sci. Instrum. **85**, 033506 (2014)]. The background plasma parameters are measured, and the ion saturation current fluctuations are characterized in terms of power spectral density to identify the dominant coherent modes and their spatial localization. A statistical approach is implemented to determine the mode spectral properties by computing the statistical dispersion relation. The poloidal wave number k_θ and the toroidal wave number k_ϕ are obtained, as well as the corresponding mode numbers. A three-dimensional linear code based on the drift-reduced Braginskii equations is used to investigate the nature of the instabilities. The linear analysis suggests a dominant ballooning character of the modes. © 2014 AIP Publishing LLC.

[<http://dx.doi.org/10.1063/1.4904808>]

I. INTRODUCTION

Energy and particle radial transport, at rates much higher than those predicted by simple collisional diffusion, is an issue affecting all fusion oriented magnetic devices.^{1,2} A deep understanding of plasma instabilities responsible for this anomalous process is needed, from their linear evolution to the highly turbulent non-linearly saturated state. While turbulent fluctuations occur on a wide range of spatio-temporal scales, a key role is played by plasma fluctuations with a frequency lower than the ion cyclotron frequency. The study of these turbulent processes in tokamaks, as well as in stellarators, is hampered by the high temperatures and densities, allowing direct measurements with fast reciprocating Langmuir probes only in a narrow portion at the edge of the plasma volume. Basic plasma physics experiments^{3–7} offer an alternative solution for turbulence studies, allowing a much easier diagnostic access, due to lower temperature and density plasmas.

In the past, a comprehensive study of plasma fluctuations has been conducted on the TORoidal Plasma EXperiment (TORPEX)⁸ in the Simple Magnetized Torus geometry (SMT). This results from the superposition of a dominant toroidal field with a much smaller vertical field. The SMT exhibit the main features of the Scrape-Off Layer (SOL), namely, pressure gradients, curvature, and gradients of the magnetic field. The covered topics range from the investigation of electrostatic instabilities,⁹ intermittent events birth and dynamics,¹⁰ and supra-thermal ion interaction with turbulence.¹¹ A simulation work validated on experimental data¹² has revealed that different instability regimes can be explored on TORPEX varying the amplitude of the vertical magnetic field. Ideal interchange modes develop for a high vertical

magnetic field component, corresponding to a short connection length. Once the number of toroidal turns performed by the open helical field lines is increased, resistive interchange modes start to dominate.¹³

To better mimic the tokamak SOL and being able to investigate the plasma core and the transition region between closed and open flux surfaces, a system consisting of an in-vessel toroidal copper conductor (TC) was recently installed on TORPEX.¹⁶ This technical solution was originally explored in the framework of nuclear fusion research^{14,15} and then abandoned due to the poor performance as a confinement device. A current generating a poloidal magnetic field is driven by applying a voltage at the two extremes of the conductor. Together with the main toroidal component, the poloidal field allows closing the flux surfaces, including a rotational transform in the TORPEX magnetic configuration. More complex magnetic geometries are accessible too, such as X-points or magnetic snowflakes.

This work is devoted to the spectral characterization of electrostatic coherent fluctuations in TORPEX plasmas, in the presence of closed field lines. We focus on a particular set of operational parameters, performing a scan in the poloidal field intensity. To assess the nature of the dominant instabilities, the first step in the experiments-simulations comparison is performed using a linear drift-reduced Braginskii solver.¹⁷

The paper outline is the following: Sec. II is dedicated to the introduction of the experimental set-up and control parameters. In Sec. III, the main background plasma parameters, namely, electron density n_e , electron temperature T_e , and plasma potential V_{pl} , are presented. In Sec. IV, we discuss ion saturation current (I_{sat}) fluctuations, focusing on the spectral characterization of the coherent modes, computing the poloidal and toroidal wave numbers, respectively, k_θ and k_ϕ , and the corresponding poloidal (m) and toroidal (n) mode numbers. In Sec. V, the results of the theoretical

^{a)}fabio.avino@epfl.ch

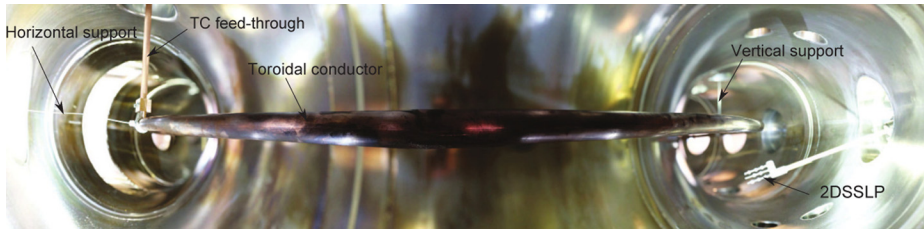


FIG. 1. Internal view of the TORPEX vacuum chamber with the TC suspended in the center of the poloidal cross section via lateral and horizontal stainless steel wires.

investigation, aimed at determining the nature of the measured instabilities using a linear approach, are presented. Finally, the conclusions and an outlook of future experiments are given in Sec. VI.

II. EXPERIMENTAL SET-UP AND CONTROL PARAMETERS

The experiments are performed on TORPEX,¹⁸ major radius $R = 1$ m and minor radius $a = 0.2$ m, with the TC suspended in the middle of the vacuum chamber (Fig. 1). A main toroidal field oriented in the counter-clockwise direction from a top view is used. A value of $B_{\phi,0} \simeq 78.7$ mT in the center of the chamber corresponds to a radial position of the Electron Cyclotron (EC) resonance layer of $r_{EC} \simeq -10$ cm. Here, the plasma breakdown is obtained using 2.45 GHz microwaves injected with a magnetron capable of reaching powers up to 10 kW.¹⁹ The main plasma production is localized around the upper hybrid resonance layer.

Hydrogen plasmas are investigated, with a constant neutral gas pressure of 1.8×10^{-4} mbar. A flat-top pulse of the plasma current lasts for about 1 s (Fig. 2). During this phase, the TC current is constant within 1%. The analysis of the probe time traces is restricted to a time window of about 800 ms when the injected magnetron power is constant at $P_{inj} \simeq 300$ W, during the flat-top of the TC current I_{TC} (Fig. 2). A range of I_{TC} between 400 A and 800 A is explored, adding to the resulting poloidal magnetic field a small vertical components to obtain quasi-concentric flux surfaces on most of the plasma volume, as indicated in Fig. 3(a). The corresponding range of safety factor values is shown in Fig. 3(b), where $q(r)$ is the value averaged over a poloidal turn along the magnetic field lines computed on the basis of the measured coil currents. An extensive set of Langmuir Probes (LPs) with an acquisition frequency of 250 kHz is implemented for

the measurements, including different arrangements to capture two-dimensional information on the poloidal cross section or to perform more refined radial scans. A set of movable LPs includes: TWIN-1 (Fig. 4(a)), a single pin LP, 2DSSLP (Fig. 4(b)), a 2D array of 8 single-sided LPs with a radial separation of 1.5 cm, SLP (Fig. 4(c)), a vertical array of eight LPs 1.8 cm separated, and FRIPLE²⁰ (Fig. 4(d)), a five tip triple probe, with 4 mm of separation between the probes. These diagnostics, located at different toroidal positions, allow computing the toroidal wave number k_{ϕ} by applying the two-point correlation technique,^{21,22} as explained in more detail in Sec. IV. Time averaged radial profiles at $z = 0$ cm of n_e , T_e , and V_{pl} are obtained by using the LPs in swept mode. The fixed LPs include the HEXagonal Turbulence Imaging Probe (HEXTIP),²³ a 2D pattern of 85 LPs separated by 3.5 cm, covering the whole poloidal cross section of TORPEX, and the Field-Aligned Probe Array (FAPA) shown in Fig. 4(e). This allows measuring the poloidal wave number k_{θ} with 44 LPs poloidally aligned along the concentric flux surfaces at four different radial positions with 1 cm separation.

III. BACKGROUND PLASMA PROFILES

The background radial profiles of n_e , T_e , and V_{pl} are measured on the low-field side (LFS) at $z = 0$ cm with a spatial resolution of 0.5 cm, using the 2DSSLP. The probe is radially moved between discharges. The applied voltage is swept at a frequency of 330 Hz between -40 V and 20 V, to cover both the ion and electron saturation regimes. The plasma potential profiles are evaluated from²⁴ $V_{pl} = V_f + \mu T_e/e$, with $\mu = 3.15$. The results are shown in Fig. 5 for the different values of currents. The measured density is in the range of $(2 - 10) \times 10^{15} \text{ m}^{-3}$. The plasma potential reaches 8 V in the center and the maximum electron temperature is about 5 eV. It can be seen that n_e , T_e , and V_{pl} peak toward the vacuum vessel central region of higher poloidal magnetic field. The position of the maximum density gradient moves radially outwards by increasing the TC current. The 2D time-averaged poloidal I_{sat} measurements are shown in Figs. 6(a) and 6(b) for the discharges with $I_{TC} \simeq 460$ A and $I_{TC} \simeq 610$ A, respectively. The plasma shape matches qualitatively the simulated magnetic flux surfaces, especially for the case at $I_{TC} \simeq 610$ A, as can be seen from the radial cuts at four poloidal angles in Fig. 6(d). For the lower value of current, a slight asymmetry can be observed in Figs. 6(a)–6(c) along the poloidal direction. Although the origin of this asymmetry is not clear, we should note that our experiment includes potential sources of poloidal asymmetries, such as the lateral and vertical TC supports, as well as the TC feed-through.

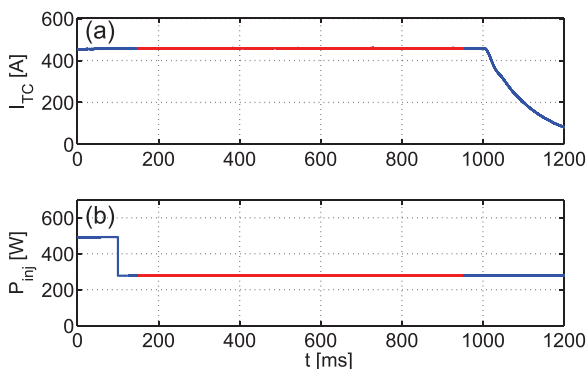


FIG. 2. I_{TC} (a) and P_{inj} (b) time traces. In red the analysed time window is highlighted.

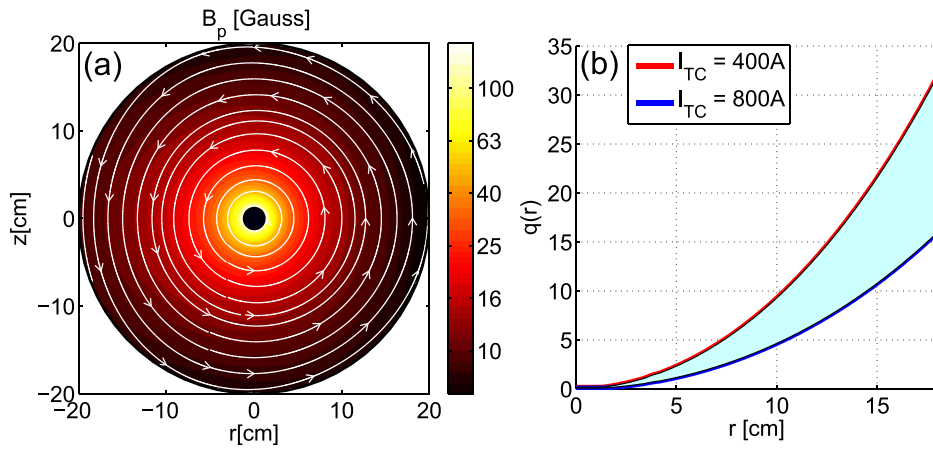


FIG. 3. (a) Example of concentric quasi-circular field lines obtained with $I_{TC}=800$ A and a vertical field coils current of 9 A. (b) In light blue the region of values of the explored safety factor radial profiles $q(r)$ is indicated.

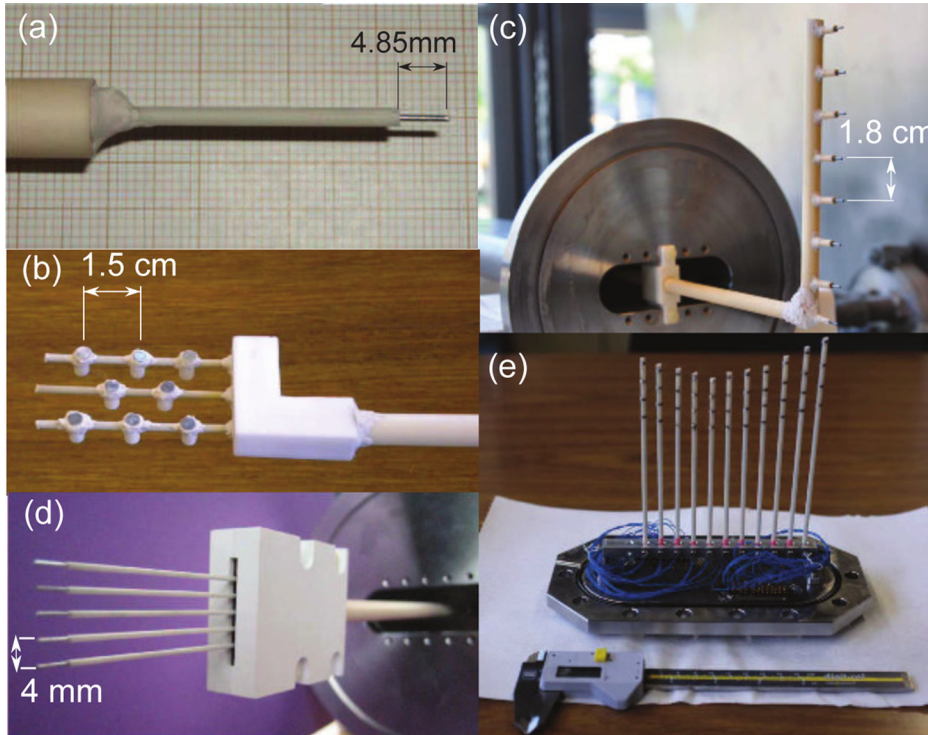


FIG. 4. (a) TWIN-1; (b) 2DSSLP; (c) SLP; (d) FRIPLE; and (e) FAPA.

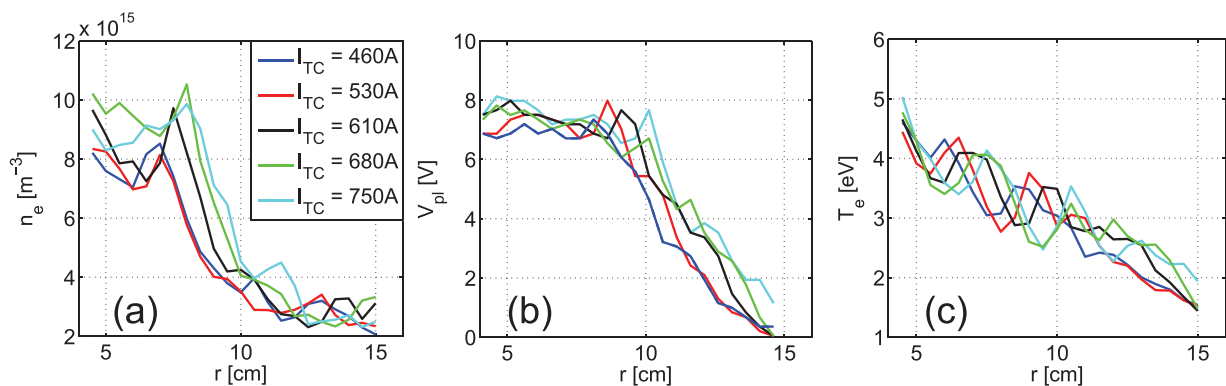


FIG. 5. LFS radial profiles at $z=0$ cm of: (a) n_e , (b) V_{pl} , and (c) T_e calculated from the measured I-V curves using the probe #08 of the 2DSSLP for the five values of toroidal conductor current.

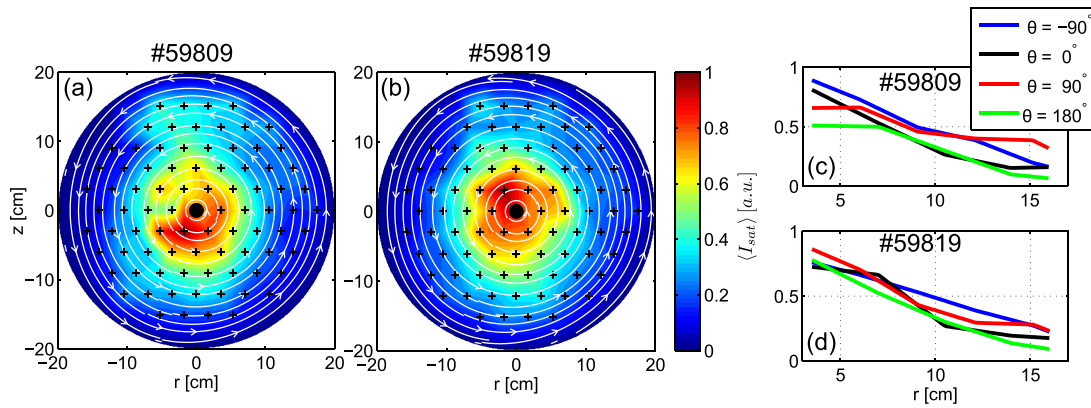


FIG. 6. Time-averaged 2D density profiles calculated from the HEXTIP I_{sat} signals, for the discharge (a) with $I_{TC} = 460$ A and (b) with $I_{TC} = 610$ A; the simulated magnetic field lines are shown in white, the black crosses represent the HEXTIP probes positions, and the toroidal conductor is represented with a black circle in the middle of the cross section. (c) and (d) I_{sat} radial cuts for different poloidal angles for the discharges with, respectively, $I_{TC} = 460$ A and $I_{TC} = 610$ A. $\theta = 0^\circ$ corresponds to the profile at $z = 0$ cm on the LFS, moving then counter-clockwise.

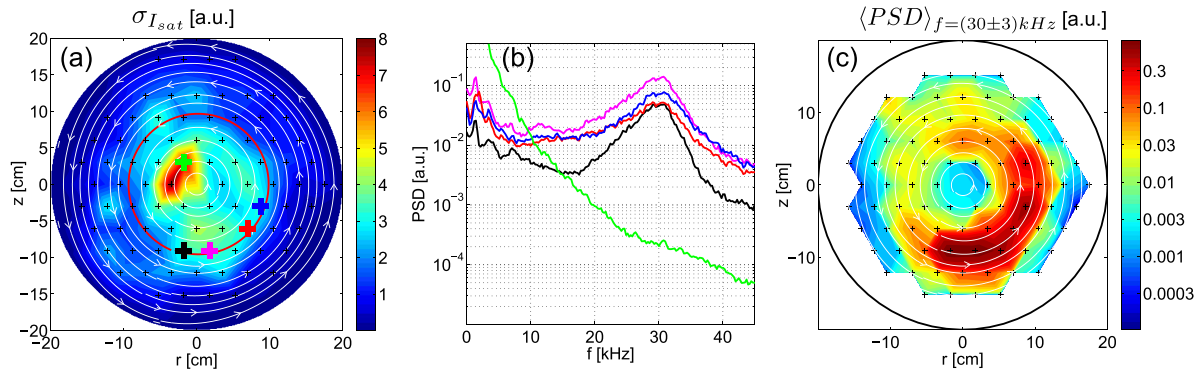


FIG. 7. HEXTIP data for the discharge #59809 at 460 A. (a) Standard deviation of the measured I_{sat} time traces; the coloured crosses correspond to the probes for which the PSD is shown in (b). (c) Mode intensity averaged on a frequency window of 3 kHz around the dominant mode frequency. The red line in (a) corresponds to the flux surface where the maximum of the PSD is measured.

IV. FLUCTUATION MEASUREMENTS

In this section, we focus on plasma fluctuation measurements, starting with the identification of the dominant quasi-coherent modes, and moving subsequently to the estimate of the toroidal and poloidal wave numbers.

A. Dominant quasi-coherent modes identification

The spatial region where the plasma fluctuations are localized on the poloidal cross section is obtained by calculating the standard deviation of HEXTIP I_{sat} signals. The resulting profiles for the discharge at 460 A are shown in Fig. 7(a). The power spectral density (PSD) of each probe signal is computed to discriminate quasi-coherent structures from broad-band fluctuations. This is illustrated in Fig. 7(b) for the four probes highlighted with coloured crosses in Fig. 7(a), indicating a dominant quasi-coherent mode at a frequency of about 30 kHz. This mode is the main focus of our investigations, since the two LPs close to the TC in Fig. 7(a) at $(r = -3.5, z = 0)$ cm and $(r = -1.75, z = 3)$ cm, even if with a higher level of fluctuations, present a much broader spectra without any coherent peak at 30 kHz. A qualitative identification of the mode poloidal position is obtained from the intensity of the mode from the PSDs of all HEXTIP

signals. The mode intensity has been calculated by averaging the PSD on a window of ± 3 kHz around the dominant mode frequency. The result for the case of 460 A is shown in Fig. 7(c), indicating a mode poloidally asymmetric, mainly localized on the bottom of the LFS, on the flux surface indicated in red in Fig. 7(a). The same features are observed for the other current values. The Gaussian fit of the PSD with the highest mode intensity provides a first indication of the mode frequency f and spectral width σ_f , as illustrated in Table I for the different TC currents. A more precise estimate of the mode radial position at $z = 0$ cm is obtained using the movable probes and evaluating at each spatial step the maximum of the PSD fitted with a Gaussian. The radial width σ_r is given by the FWHM of a Gaussian fit performed

TABLE I. Frequency f , spectral width σ_f , radial position r_m , and radial width σ_{r_m} of the dominant mode for different TC currents I_{TC} .

I_{TC} (A)	f (kHz)	σ_f (kHz)	r_m (cm)	σ_{r_m} (cm)
460	29.8	2.4	9.0	1.2
530	29.1	2.9	9.8	1.1
610	26.8	2.4	10.5	1.0
680	23.2	2.2	10.9	1.3
750	22.8	1.0	11.2	0.9

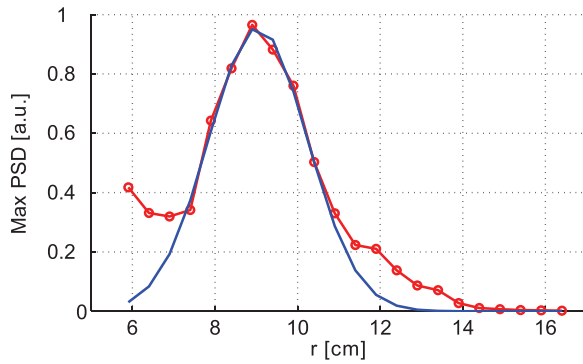


FIG. 8. Radial scan of the PSD maximum on I_{sat} signals (red), fitted with a Gaussian function (blue), for $I_{TC} = 460$ A.

on the radial profile of the PSD maxima (Fig. 8). The results are summarized in Table I. The data indicate that the mode moves slightly outward when the TC current is increased. This is consistent with the shift of the position of the maximum gradient of the pressure.

B. Wave number and mode number measurements

To measure the toroidal wave number k_ϕ , the four LPs previously introduced in Sec. II have been placed at different toroidal locations ϕ but at the same radial position r . Based on the results of Table I, the chosen values are $r = [9.5, 10, 10.5, 11, 11.5]$ cm for the values of current, respectively, $I_{TC} = [460, 530, 610, 680, 750]$ A. The arrangement is schematically shown in Fig. 9(a). k_ϕ has been

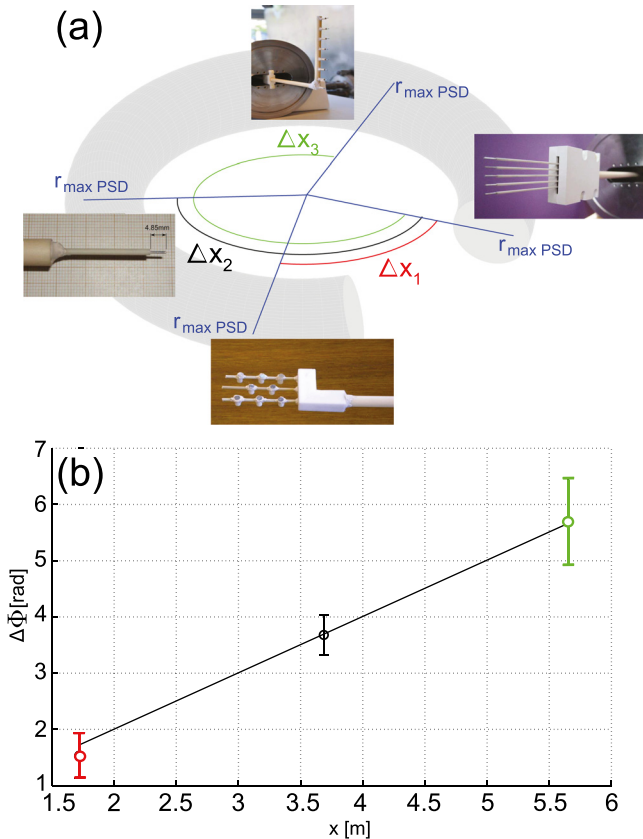


FIG. 9. (a) Schematic view of the probe locations. (b) Linear fit on the phase shift of consecutive probe couples for the k_ϕ estimate.

TABLE II. Toroidal wave number k_ϕ and mode number for the explored values of TC current.

I_{TC} (A)	k_ϕ (1/m)	σ_{k_ϕ} (1/m)	n
460	1.05	0.22	1.15 ± 0.22
530	1.17	0.86	1.29 ± 0.86
610	1.14	0.20	1.26 ± 0.20
680	1.14	0.38	1.27 ± 0.38
750	1.27	0.87	1.42 ± 0.87

estimated by applying the two-point correlation technique between FRIPLE and the other probes, obtaining the phase shift Φ from the statistical dispersion relation (SDR). The toroidal wave number $k_\phi = d(\Delta\Phi)/dx$ is computed as the angular coefficient of the linear fit on $\Phi(x)$, where $x = R\phi$ is the probe distance from the reference one along the toroidal direction (Fig. 9). The calculated wave numbers k_ϕ are shown in Table II, together with the corresponding mode numbers n . These are computed from the radial position of the probes R as $n = 2\pi R/\lambda_\phi = Rk_\phi$, indicating $n = 1$ modes for the investigated plasmas as illustrated in Fig. 10. The σ_{k_ϕ} is the uncertainty on the fit result with 95% confidence, while the uncertainty on n is obtained with the statistical propagation of errors.

To measure the poloidal mode number m , the FAPA diagnostic presented in Sec. II was used. We note that the explored values of TC current, namely, $I_{TC} = [450, 500, 550, 600, 650]$ A, cover a smaller range with respect to the ones in Table II. This is due to the fact that for currents higher than 650 A, the mode moves outside the spatial region covered by FAPA, which is composed of fixed LPs. For each value of I_{TC} , the poloidal row (PR) with the largest mode intensity is selected, as can be seen in Fig. 11 for the case $I_{TC} \simeq 450$ A, in which the mode is localized on the third PR starting from the bottom. For the cases where two adjacent PRs have comparable mode intensity, the one where the mode appears first on the poloidal cross section is considered, namely, the PR with the first probe detecting it having the smaller radial position. The phase-shift is computed with respect to the first LP on the high-field-side. Since the LP locations range from -4 cm to 6 cm, the transformed poloidal angle $\theta^* = \theta - \epsilon \sin \theta$ value is computed²⁵ to take into account the toroidal magnetic field variation along the PR to the first order of the inverse aspect ratio ϵ . The poloidal mode number is

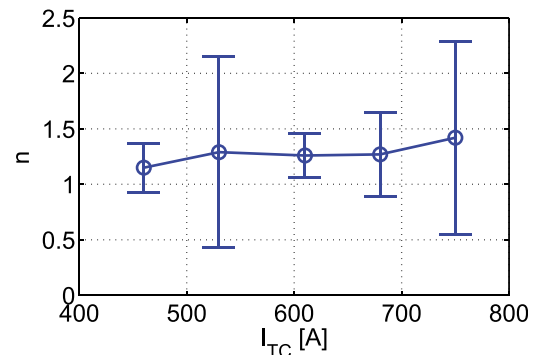


FIG. 10. Toroidal mode number n as a function of the current I_{TC} .

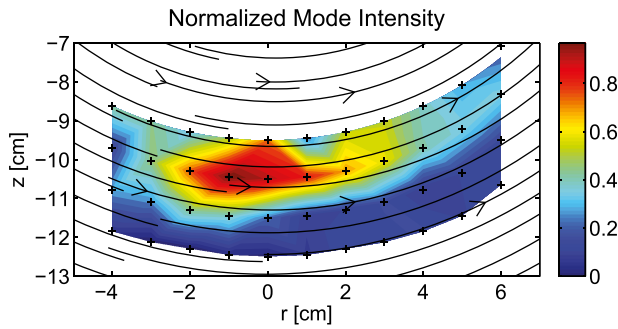


FIG. 11. Normalized mode intensity on the FAPA for a discharge with $I_{TC} \simeq 450$ A. The black crosses correspond to the FAPA probes, while the black lines and arrows are the simulated magnetic field lines.

then given by a linear fit on the phase shift $\Delta\Phi(\theta^*)$. We remark that the PR where the mode intensity is the largest moves outward as the TC current is increased, confirming the mode radial position measured at $z=0$ (Table I). Table III and Fig. 12 summarise the results of this analysis.

To verify the field aligned character of the analysed coherent modes, the safety factor values at the position of the analysed PR ($q(z_C)$), averaged on the corresponding flux surface, are calculated for each value of I_{TC} . However, the estimate of the q values to be compared to the measured m is affected by several factors: the mode width, the uncertainty on the LP positions and on the TC position. To account for this, the q error-bars have been estimated as the range of value the safety-factor takes moving ± 1 cm radially from the PR radial position. The results are shown in Fig. 12, indicating the field-aligned character of the investigated instability.

C. Poloidal rotation

A qualitative insight on the mode dynamics is obtained by applying the Conditional Average Sampling technique (CAS)^{26,27} to the HEXTIP data. The poloidal rotation of the mode within the selected time window of $100 \mu\text{s}$ for the CAS analysis is evident in Fig. 13, where a few snapshots are shown for the discharge with $I_{TC} \simeq 610$ A, using as trigger the HEXTIP probe at $r = 10.5$ cm and $z = 0$ cm.

The experimental poloidal velocity in the laboratory frame v_{exp} is counter-clockwise, resulting from the sum of electron diamagnetic velocity v_{de} (clockwise) and the $\mathbf{E} \times \mathbf{B}$ velocity $v_{\mathbf{E} \times \mathbf{B}}$ (counter-clockwise), defined as

$$\mathbf{v}_{\mathbf{E} \times \mathbf{B}} = \frac{\mathbf{E} \times \mathbf{B}}{B^2} \quad \mathbf{v}_{\text{de}} = \frac{T_e}{eB_\phi^2} \frac{\nabla n_e}{n_e} \times \mathbf{B}_\phi. \quad (1)$$

TABLE III. Poloidal mode number m and flux-surface averaged safety factor q for the explored values of TC current.

I_{TC} (A)	z_C (cm)	m	σ_m	q	σ_q
450	10.5	10.54	0.22	9.5	1.8
500	10.5	10.37	0.27	8.6	1.7
550	11.5	10.87	0.52	9.3	1.6
600	11.5	9.86	0.32	8.6	1.5
650	12.5	11.46	0.59	9.5	1.5

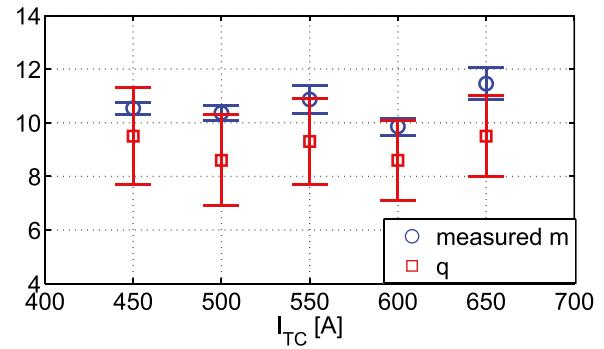


FIG. 12. Poloidal mode number m (blue circles) and corresponding flux-surface averaged safety factor (red squares) for the investigated toroidal conductor currents I_{TC} .

The measured mode frequency $f = (26.8 \pm 2.4)$ kHz is used for the estimate. The poloidal wave number is obtained from the poloidal mode number $m = (9.86 \pm 0.32)$, calculated for the current at 600 A

$$k_\theta = \frac{m}{r} = (93.9 \pm 9.4) \text{ m}^{-1}. \quad (2)$$

An electron temperature $T_e \simeq 3$ eV and magnetic field $B_\phi \simeq 78.7$ mT are considered. From the density and plasma potential radial profiles, we can obtain, respectively, a density scale length $L_n = |\nabla n_e / n_e|^{-1} \simeq 4$ cm and electric field $E = -\nabla V_{pl} \simeq 240$ V/m at the radial position of the mode. It follows that:

$$|\mathbf{v}_{\text{exp}}| = \frac{2\pi f}{k_\theta} = (1.78 \pm 0.24) \text{ km/s},$$

$$|\mathbf{v}_{\mathbf{E} \times \mathbf{B}}| = \frac{E}{B_\phi} \simeq 3 \text{ km/s}, \quad |\mathbf{v}_{\text{de}}| = \frac{T_e}{B_\phi L_{n_e}} \simeq 1 \text{ km/s}, \quad (3)$$

which is consistent with the Doppler shift

$$|\mathbf{v}_{\text{exp}}| = |\mathbf{v}_{\mathbf{E} \times \mathbf{B}}| - |\mathbf{v}_{\text{de}}|.$$

Moreover, the consistency with the results of the CAS of Fig. 13 could be verified. We note that the mode peak covers in $\Delta t = 20 \mu\text{s}$ a spatial distance $\Delta x \simeq 3.5$ cm (rotating in the poloidal counter clock-wise direction), which corresponds to the two HEXTIP probes indicated by the white crosses in Figs. 13(c) and 13(d). This results in an estimate of the poloidal mode speed of about

$$|\mathbf{v}| = \frac{\Delta x}{\Delta t} = \frac{3.5 \text{ cm}}{20 \mu\text{s}} \simeq 1.75 \text{ km/s}, \quad (4)$$

which is in agreement with the measured speed $|\mathbf{v}_{\text{exp}}| \simeq 1.78$ km/s of Eq. (1) within the experimental uncertainties.

The change in the mode poloidal rotation for a reversed toroidal field (clock-wise direction from a top view), implying a reversed $\vec{E} \times \vec{B}$ velocity, has been qualitatively investigated. The mode poloidally rotates clock-wise in the laboratory frame, confirming the dominant role of the $\mathbf{v}_{\mathbf{E} \times \mathbf{B}}$, and it is mainly localized in the upper part of the LFS.

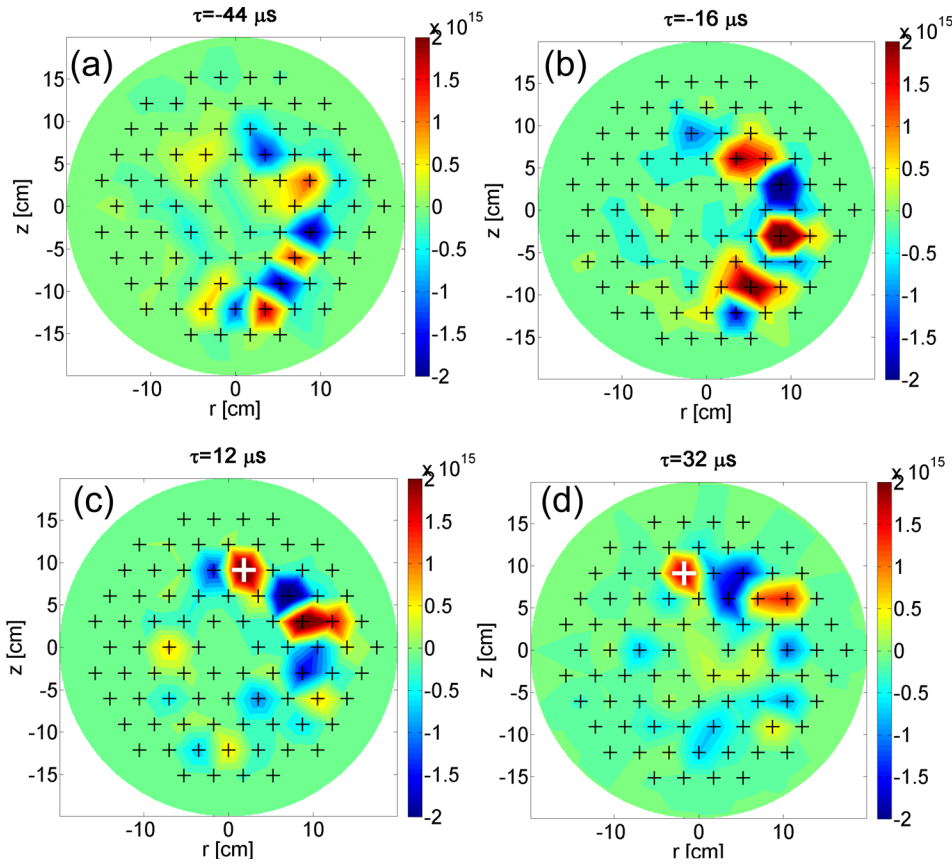


FIG. 13. Snapshots of the resulting CAS technique applied on HEXTIP data for the discharge #59819 with $I_{TC} \simeq 610$ A, taking as reference the probe at $(r = 10.5, z = 0)$ cm. $\tau = 0$ μ s corresponds to the detection time of the events above the chosen threshold.

V. DRIVING MECHANISM OF THE DOMINANT QUASI-COHERENT MODES

As a first step to understand the experimental measurements, we investigate the nature of the modes that are unstable in the considered configurations using a set of linearised drift-reduced Braginskii equations.²⁸ These are solved using the numerical code presented in Ref. 25. In the limit of cold ions ($T_i = 0$), neglecting the stress tensor and the electromagnetic effects, the equations for the perturbed electron density, n_e , electron parallel velocity $V_{\parallel e}$, potential, Φ , electron temperature T_e , and ion parallel velocity $V_{\parallel i}$ can be written as³⁰

$$\begin{aligned}
 \frac{\partial n_e}{\partial t} &= \frac{R}{L_n} \frac{\hat{P}^L(\Phi)}{B} + 2 \frac{\hat{C}^L}{B} (T_e + n_e - \Phi) \\
 &\quad - (\nabla_{\parallel} + \nabla \cdot \mathbf{b}) V_{\parallel e}, \\
 \frac{1}{B^2} \frac{\partial \nabla_{\perp}^2 \Phi}{\partial t} &= 2 \frac{\hat{C}^L}{B} (n_e + T_e) + (\nabla_{\parallel} + \nabla \cdot \mathbf{b}) (V_{\parallel i} - V_{\parallel e}), \\
 \frac{m_e}{m_i} \frac{\partial V_{\parallel e}}{\partial t} &= \nu (V_{\parallel i} - V_{\parallel e}) + \nabla_{\parallel} (\Phi - n_e - 1.71 T_e), \\
 \frac{\partial T_e}{\partial t} &= \frac{\eta}{B L_n} \hat{P}^L(\Phi) + \frac{4 \hat{C}^L}{3 B} \left(\frac{7}{2} T_e + n_e - \Phi \right) \\
 &\quad + \frac{2}{3} (\nabla_{\parallel} + \nabla \cdot \mathbf{b}) (0.71 V_{\parallel i} - 1.71 V_{\parallel e}), \\
 \frac{\partial V_{\parallel i}}{\partial t} &= -\nabla_{\parallel} (n_e + T_e).
 \end{aligned} \tag{5}$$

Here, R is the major radius, L_n and L_T are the radial scale lengths of, respectively, the background density and

temperature, B is the modulus of the magnetic field, ν is the normalized parallel resistivity, and $\eta = L_n/L_T$. \hat{P}^L and \hat{C}^L are, respectively, the linearised Poisson bracket and curvature operator (see Ref. 26 for the complete expressions). For our calculations, we consider the radial position of the mode, $a = 0.1$ m, the density and temperature scale lengths, respectively, $L_n = 4$ cm and $L_T = 10.5$ cm, plasma resistivity $\nu = 6 \times 10^{-3}$ in c_s/R_0 units, toroidal mode number $n = 1$, magnetic shear $\hat{s} = 2$, and safety factor $q = 9$, as obtained from the experimental measurements.

The dominant linear growth rate γ is evaluated using several physical models. First, the complete set of Eq. (5) (full model) is implemented. Then, the same analysis is performed using four reduced models,²⁹ where n , ϕ , $V_{\parallel e}$, and T_e are evolved, neglecting the parallel ion velocity $V_{\parallel i}$, and therefore the coupling with the ion sound waves. These models include the resistive and inertial branches of the ballooning modes (BM) and of the drift waves (DW). In the BM models, \hat{C}^L is only kept in the vorticity equation, $\nabla_{\parallel} n$ and $\nabla_{\parallel} T_e$ are neglected in the electron velocity equation, and $V_{\parallel e}$ is neglected in both the density and temperature equations. In the DW models, \hat{C}^L is set to zero for all the fields. For both BM and DW, the resistive (RBM) and inertial (InBM and InDW) branches are obtained by neglecting, respectively, the inertial term ($m_e/m_i \partial V_{\parallel e}/\partial t$) and the resistive one ($-\nu V_{\parallel e}$).

The results are shown in Table IV and suggest the dominant character of the curvature term in determining the mode linear growth-rate. We can therefore infer the ballooning character of the instabilities for the investigated plasma

TABLE IV. Growth rate for a toroidal wave number $n = 1, m = 9$ using the following models: full model (Full), resistive and inertial ballooning model (respectively, RBM and InBM), resistive and inertial drift waves model (respectively, RDW and InDW).

Model	Full	RBM	InBM	RDW	InDW
γ	3.2	3.5	3.4	0.1	0

parameters, which is consistent with the poloidal localization of the mode mainly on the LFS, where the curvature plays a destabilizing effect. However, we cannot discriminate between the resistive and the inertial branch.

Non-linear simulations will be developed to further address the study of the instability nature.

VI. CONCLUSIONS

The investigation of plasma fluctuations and coherent modes in the quasi-circular, closed flux surface configuration of the TORPEX device is presented. The poloidal field intensity is changed by varying the toroidal conductor current in the range of 450–750 A. The background 1D radial profiles of n_e , T_e , and V_{pl} are reconstructed, together with the 2D data of n_e . The dominant frequencies of coherent plasma fluctuations are identified and localized on the poloidal cross section. A spectral analysis of the coherent modes is performed, measuring the poloidal and toroidal wave number and mode number. The field-aligned feature of the mode is verified. The asymmetric poloidal localization of the plasma coherent structures suggests a ballooning character, which is confirmed by the theoretical analysis.

Further investigations will be performed to explore the dependence of plasma fluctuations on experimental parameters, such as different neutral pressures or gases. The use of the non-linear simulations is foreseen.

ACKNOWLEDGMENTS

This work was supported in part by the Swiss National Science Foundation. This project has received funding from the European Union's Horizon 2020 research and innovation programme under Grant Agreement No. 633053. The views and opinions expressed herein do not necessarily reflect those of the European Commission.

The authors wish to acknowledge the very helpful discussions with the CRPP colleagues A. Bovet, F. Halpern,

and A. Masetto and the support of the CRPP technical team.

- ¹W. Horton, *Rev. Mod. Phys.* **71**, 735 (1999).
- ²O. E. Garcia, J. Horacek, R. A. Pitts, A. H. Nielsen, W. Fundamenski, J. P. Graves, V. Naulin, and J. Juul Rasmussen, *Plasma Phys. Controlled Fusion* **48**, L1–L10 (2006).
- ³C. Riccardi, D. Xuantong, M. Salierno, L. Gamberale, and M. Fontanesi, *Phys. Plasmas* **4**, 3749 (1997).
- ⁴C. Riccardi and A. Fredriksen, *Phys. Plasmas* **8**, 199 (2001).
- ⁵A. Fasoli, B. Labit, M. McGrath, S. H. Müller, G. Plyushchev, M. Podestà, and F. M. Poli, *Phys. Plasmas* **13**, 055902 (2006).
- ⁶K. W. Gentle and H. He, *Plasma Sci. Technol.* **10**(3), 284 (2008).
- ⁷Th. Pierre, *Rev. Sci. Instrum.* **84**, 013504 (2013).
- ⁸A. Fasoli, F. Avino, A. Bovet, I. Furno, K. Gustafson, S. Jolliet, J. Loizu, D. Malinverni, P. Ricci, F. Riva, C. Theiler, M. Spolaore, and N. Vianello, *Nucl. Fusion* **53**, 063013 (2013).
- ⁹A. Fasoli, A. Burckel, L. Federspiel, I. Furno, K. Gustafson, D. Iraj, B. Labit, J. Loizu, G. Plyushchev, P. Ricci, C. Theiler, A. Diallo, S. H. Müller, M. Podestà, and F. Poli, *Plasma Phys. Controlled Fusion* **52**, 124020 (2010).
- ¹⁰C. Theiler, I. Furno, P. Ricci, A. Fasoli, B. Labit, S. H. Müller, and G. Plyushchev, *Phys. Rev. Lett.* **103**, 065001 (2009).
- ¹¹A. Bovet, I. Furno, A. Fasoli, K. Gustafson, and P. Ricci, *Plasma Phys. Controlled Fusion* **55**, 124021 (2013).
- ¹²P. Ricci, C. Theiler, A. Fasoli, I. Furno, K. Gustafson, D. Iraj, and J. Loizu, *Phys. Plasmas* **18**, 032109 (2011).
- ¹³P. Ricci and B. N. Rogers, *Phys. Rev. Lett.* **104**, 145001 (2010).
- ¹⁴B. Lehnert, *Plasma Phys.* **10**, 281 (1968).
- ¹⁵S. Skellett, *Cryogenics* **15**, 563 (1975).
- ¹⁶F. Avino, A. Fasoli, and I. Furno, *Rev. Sci. Instrum.* **85**, 033506 (2014).
- ¹⁷P. Ricci and B. N. Rogers, *Phys. Plasmas* **16**, 092307 (2009).
- ¹⁸A. Fasoli, A. Burckel, L. Federspiel, I. Furno, K. Gustafson, D. Iraj, B. Labit, J. Loizu, G. Plyushchev, P. Ricci, C. Theiler, A. Diallo, S. H. Müller, M. Podestà, and F. Poli, *Plasma Phys. Controlled Fusion* **52**, 124020 (2010).
- ¹⁹M. Podestà, A. Fasoli, B. Labit, M. McGrath, S. Müller, and F. M. Poli, *Plasma Phys. Controlled Fusion* **47**, 1989 (2005).
- ²⁰C. Theiler, I. Furno, A. Kuenlin, Ph. Marmillod, and A. Fasoli, *Rev. Sci. Instrum.* **82**, 013504 (2011).
- ²¹J. M. Beall, Y. C. Kim, and E. J. Powers, *J. Appl. Phys.* **53**, 3933 (1982).
- ²²F. M. Poli, S. Brunner, A. Diallo, A. Fasoli, I. Furno, B. Labit, S. H. Müller, G. Plyushchev, and M. Podestà, *Phys. Plasmas* **13**, 102104 (2006).
- ²³S. H. Müller, A. Fasoli, B. Labit, M. McGrath, O. Pisaturo, G. Plyushchev, M. Podestà, and F. M. Poli, *Phys. Plasmas* **12**, 090906 (2005).
- ²⁴F. F. Chen, *Introduction to Plasma Physics and Controlled Fusion* (Springer, 2006).
- ²⁵O. Klüber, H. Zohm, H. Bruhns, J. Gernhardt, A. Kallenbach, and H. P. Zehrfeld, *Nucl. Fusion* **31**, 907 (1991).
- ²⁶H. Johnsen, H. L. Pecseli, and J. Trulsen, *Phys. Fluids* **30**, 2239 (1987).
- ²⁷I. Furno, B. Labit, M. Podestà, A. Fasoli, S. H. Müller, F. M. Poli, P. Ricci, C. Theiler, S. Brunner, A. Diallo, and J. Graves, *Phys. Rev. Lett.* **100**, 055004 (2008).
- ²⁸S. I. Braginskii, *Rev. Plasma Phys.* **1**, 205 (1965).
- ²⁹A. Masetto, F. D. Halpern, S. Jolliet, and P. Ricci, *Phys. Plasmas* **19**, 112103 (2012).
- ³⁰S. Jolliet, F. Halpern, J. Loizu, A. Masetto, and P. Ricci, *Phys. Plasmas* **21**, 022303 (2014).